Inorganic Chemistry

pubs.acs.org/IC

Article

Crystal Growth and Physical Properties of Hybrid CoSn−YCo_6Ge_6 Structure Type $Ln_xCo_3(Ge_{1-y}Sn_y)_3$ (Ln = Y, Gd)

Moisés Bravo, Gregory T. McCandless, Ryan E. Baumbach, Yaojia Wang, Mazhar N. Ali, and Julia Y. Chan*

Cite This: *Inorg. Chem.* 2023, 62, 18049−18055

Read Online

ACCESS | Metrics & More | Article Recommendations | Supporting Information

ABSTRACT: There is an ongoing interest in kagome materials because they offer tunable platforms at the intersection of magnetism and electron correlation. Herein, we examine single crystals of new kagome materials, $Ln_xCo_3(Ge_{1-y}Sn_y)_3$ (Ln = Y, Gd; y = 0.11, 0.133), which were produced using the Sn flux-growth method. Unlike many of the related chemical analogues with the LnM_6X_6 formula (M = transition metal and X = Ge, Sn), the Y and Gd analogues crystallize in a hybrid YCo_6Ge_6/CoSn structure, with Sn substitution. While the Y analogue displays temperature-independent paramagnetism, magnetic measurements of the Gd analogue reveal a magnetic moment of 8.48 μ_B, indicating a contribution from both Gd and Co. Through anisotropic magnetic measurements, the direction of Co-magnetism can be inferred to be in plane with the kagome net, as the Co contribution is only along H//a. Crystal growth and structure determination of $Y_xCo_3(Ge,Sn)_3$ and $Gd_xCo_3(Ge,Sn)_3$, two new hybrid kagome materials of the CoSn and YCo_6Ge_6 structure types. Magnetic properties, heat capacity, and resistivity on single crystals are reported.

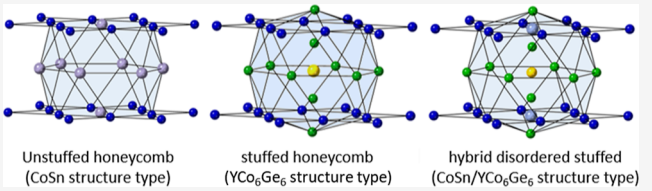

1. INTRODUCTION

The study of kagome lattice materials is an exciting topic in condensed matter due to their intrinsic geometric frustration, strong electron correlations, and electronic structure topology.[1,2] In particular, kagome materials have electronic band structure features that are symmetry protected, typically near or at the Fermi level. The kagome-derived bands are filled as flat bands (electrons with constant kinetic energy), Dirac cones (electrons avoiding a crossing point), and van Hove singularities (leading to enhanced electron−electron interactions). Among kagome materials, compounds with the formula LnM_6X_6 (Ln = lanthanide; M = transition metal, X = groups 13 and 14) host a wide range of elemental combinations and set the stage for tuning of physical properties. As there are a diverse number of elements that can be substituted and there are two independent sublattices that can host a magnetic ion, kagome materials can host complex and noncollinear magnetic states. Several Mn[3] and Fe[4] analogues order magnetically with temperatures up to 400,[5] while Cr does not order. When magnetic lanthanides are present in these analogues, the two magnetic lattices (lanthanide and transition metal) couple, leading to interesting noncollinear or ferrimagnetic behavior, manifesting in interesting spin textures.[6] $TbMn_6Sn_6$ exemplifies the exotic phenomena yielded from mixing topological electronic states and magnetism as it manifests a Chern gap.[7] The nonmagnetic Sc,[8,9] Y,[10] and Lu[11] $LnMn_6Sn_6$ analogues host diverse magnetic states dominated by the Mn sublattice, such as magnetic spin chirality, long-range double-cone spin structure, and incommensurate antiferromagnetic arrangements. However, the V and Co analogues are the only families to exhibit no magnetic contribution from the transition metal. Nonmagnetic kagome metal analogues of LnV_6Sn_6 have been identified as an ideal platform to study the interplay between lanthanide magnetism and kagome-derived band structures, such as noncollinear spin structures,[12] charge density waves,[13] and quantum critical behavior.[14] In contrast, the Co analogues have not been adequately examined: preliminary magnetic measurements of polycrystalline Co analogues have only been measured to 90 K with no indication of magnetic ordering.[15,16] Furthermore, it is important to consider that this structure may be susceptible to subtle variations (e.g., vacancies and superstructures), which would be expected to strongly affect the electronic and magnetic properties.

Recently, we discovered a new hybrid structure of the CoSn and YCo_6Ge_6 structure types $Yb_{0.5}Co_3Ge_3$.[17,18] Unusual magnetic anisotropy is observed at low temperatures for $Yb_{0.5}Co_3Ge_3$, where the magnetic susceptibility for H//c exhibits a noticeable increase near 20 K, while a similar feature is not observed when measured along H//a and is proposed to be an indication of spin canting or reorientation.[17]

Received: June 29, 2023
Revised: October 3, 2023
Accepted: October 10, 2023
Published: October 23, 2023

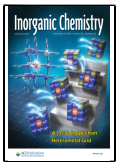

For single crystals, the effective magnetic moment of $\mu_{eff} = 4.23$ μ_B is less than the spin-only moment of Yb^{3+} (4.54 μ_B). However, magnetization for H//c (the easy axis) shows a saturation moment of ~1 μ_B at 2 K. Recently, the presence of a kink at $T \sim 95$ K in the electrical resistivity, coupled with a structural phase transition involving a change in space group from $P6/mmm$ to $P6_3/m$, was also found in $Yb_{0.5}Co_3Ge_3$.[18] The combined structural phase transition and kink in the resistivity are characteristic of charge density waves in kagome metals, similar to what is seen for FeGe[19] and AV_3Sb_5.[20] The structural distortion in $Yb_{0.5}Co_3Ge_3$ is similar to the twisting of the equilateral triangles observed in $MgCo_6Ge_6$ with the kagome nets maintaining planarity.[21] The distorted hexagons of the kagome net break two mirror planes while preserving inversion symmetry with a doubling of the unit cell along the c-axis. These results suggest that the broader $Ln_{0.5}Co_3Ge_3$ family may provide a platform for studying the complex interplay between f-electron magnetism, electronic instabilities, and structural complexity. In order to further investigate this possibility, we present the crystal growth, single-crystal structural determination, magnetic properties, heat capacity, and resistivity on the single crystalline analogues $Y_xCo_3(Ge_{1-y}Sn_y)_3$ ($x = 0.33$, $y = 0.11$) and $Gd_xCo_3(Ge_{1-y}Sn_y)_3$ ($x = 0.11$, $y = 0.133$).

2. EXPERIMENTAL SECTION

2.1. Synthesis of $Ln_xCo_3(Ge_{1-y}Sn_y)_3$ (Ln = Y, Gd; $y = 0.11$, 0.133). Single crystals of $Ln_xCo_3(Ge_{1-y}Sn_y)_3$ (Ln = Y, Gd; $y = 0.11$, 0.133) were grown by using the flux-growth method with Sn as the low melting metal flux. Elements were weighed out in the reaction ratio of 1 Ln/6 Co/6 Ge/20 Sn (Ln = Y or Gd), transferred into a Canfield crucible set, and sealed in a fused silica tube with ~1/3 atm of Argon gas. After ramping the temperature up at 100 °C/h, the Y sample was dwelled at 1175 °C for 6 h and was cooled to 500 °C at a rate of 5 °C/h. The ampule with Gd was heated to 1000 °C at a rate of 100 °C/h and dwelled for 24 h. The system was then cooled to 815 °C at a rate of 2 °C/h. Both ampules were removed, inverted, and centrifuged at 3000 rpm. The residual Sn flux was etched from the crystals using 1:1 HCl/H_2O. The synthesis of both analogues resulted in a high yield of rod-like morphology of the desired product. Single crystals up to 6 mm in length and a thickness of ~0.4 mm were grown, with examples shown in Figure 1. A small amount of the $LnCo_2Ge_2$ impurity can be visually identified and mechanically separated from the desired phase.

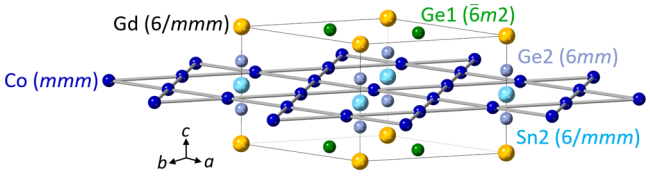

Figure 1. Single crystals of $Y_xCo_3(Ge_1Sn_y)_3$ ($x = 0.33$, $y = 0.11$) and $Gd_xCo_3(Ge_1Sn_y)_3$ ($x = 0.3$, $y = 0.133$) with composition obtained from the X-ray refined models of the single-crystal X-ray diffraction data. The orientation of the crystals was determined, where the c-axis is along the length of the crystal.

2.2. Structure Determination. The crystal structures of the compounds were determined from single-crystal fragments using a Bruker D8 Quest Kappa single-crystal X-ray diffractometer equipped with an IμS microfocus source (Mo K_α, $\lambda = 0.71073$ Å), a HELIOS optics monochromator, and a PHOTON III CPAD detector. The diffraction datasets were integrated using the Bruker SAINT program, and an absorption correction was applied to the intensities with a multiscan method in SADABS 2016/2.[22] The preliminary starting models were obtained using the intrinsic phasing method in SHELXT.[23] The indexed precession images from our datasets are available in the Supporting Information for both analogues (Figure S3).

For our preliminary structural models, Ge atoms were initially assigned to the Wyckoff sites 2c, 2e, and 1b (atomic coordinates are provided in Table 1) similar to the model previously reported in $Yb_{0.5}Co_3Ge_3$;[17] however, the 1b site had an elevated amount of residual electron density in comparison to the other residual two Ge sites. Sn was assigned at the 1b site, effectively reducing refinement statistics and residual electron density. Unlike our previously reported $Yb_{0.5}Co_3Ge_3$ model with less than 8% occupancy of Ge on the 1b site, $Y_xCo_3(Ge_{1-y}Sn_y)_3$ ($x = 0.33$, $y = 0.11$) and $Gd_xCo_3(Ge_{1-y}Sn_y)_3$ ($x = 0.3$, $y = 0.133$) have Sn occupancies of ~33 and ~40%, respectively. The occupancies of the Ln and Ge2 sites were constrained to be equivalent after the independent refinements of the Y analogue yielded statistically similar occupancies of 0.332(3) for Y and of 0.325(5) for Ge2, and the Gd analogue yielded occupancies of 0.2905(16) for Gd and of 0.292(5) for Ge2. Additionally, an EADP command was initially used on the Ge2 and Sn2 sites, where both residual electron density of 1.98 e Å^{-3} and a hole of −2.69 e Å^{-3} were present <0.50 Å away from Ge2. However, removing the command resulted in a peak of 0.56 e Å^{-3} and a hole of −0.782 e Å^{-3}. While these modeling differences are minor, the removal of the constraint yields better figures of merit and a better fit with the EDS values collected. To corroborate this observation, observed Fourier maps of the disordered regions were calculated, and there is a prolate ellipsoid for the Sn2 site and not for the Ge2 site, shown in Figure S5.

Table 1. Atomic Coordinates of $Y_{0.33}Co_3Ge_{2.67}Sn_{0.33}$ and $Gd_{0.30}Co_3Ge_{2.60}Sn_{0.40}$

atom	site	x	y	z	U_{iso}*/U_{eq}	Occ. (<1)
$Y_{0.33}Co_3Ge_{2.67}Sn_{0.33}$						
Y1	1a	0	0	0	0.0108(3)	0.3334(12)
Co1	3g	1/2	0	1/2	0.00985(13)	
Ge1	2c	1/3	2/3	0	0.00890(12)	
Ge2	2e	0	0	0.2997(5)	0.0122(2)	0.3333(12)
Sn2	1b	0	0	1/2	0.0251(6)	0.333(2)
$Gd_{0.30}Co_3Ge_{2.60}Sn_{0.40}$						
Gd1	1a	0	0	0	0.0088(2)	0.2980(11)
Co1	3g	1/2	0	1/2	0.00929(13)	
Ge1	2c	1/3	2/3	0	0.00860(13)	
Ge2	2e	0	0	0.2941(6)	0.0118(3)	0.2979(11)
Sn2	1b	0	0	1/2	0.0276(6)	0.404(2)

Crystallographic data and refinement parameters are reported in Tables S1 and S2. Data were also collected at 90 K; crystallographic data, refinement parameters, and atomic positions are provided in Tables S3 and S4.

Single crystals of $Y_{0.33}Co_3Ge_{2.67}Sn_{0.33}$ and $Gd_{0.30}Co_3Ge_{2.60}Sn_{0.40}$ were analyzed using energy-dispersive (X-ray) spectroscopy (EDS) on a VERSA 3D focused ion beam scanning electron microscope with an acceleration voltage of 20 kV and a spot size of 7 to confirm the presence of Sn in the sample. Data were collected for 5 spots on $Y_xCo_3(Ge_{1-y}Sn_y)_3$, and three area scans (13.23 × 2.86 μm) were used for $Gd_xCo_3(Ge_{1-y}Sn_y)_3$. The weight percentages obtained from EDS resulted in the atomic formulas $Y_{0.37(1)}Co_{3.00(3)}Ge_{2.61(4)}Sn_{0.39(1)}$ and $Gd_{0.31(2)}Co_{3.00(2)}Ge_{2.52(2)}Sn_{0.24(1)}$, which are in good agreement with composition from single-crystal refinements $Y_{0.33}Co_3Ge_{2.67}Sn_{0.33}$ and $Gd_{0.30}Co_3Ge_{2.60}Sn_{0.40}$, respectively. Values were normalized to Co as it does not participate in the disorder within the system. In addition, the powder diffraction data for ground single crystals are provided in Figures S2 and S3. For simplicity, $Y_{0.33}Co_3Ge_{2.67}Sn_{0.33}$ and $Gd_{0.30}Co_3Ge_{2.60}Sn_{0.40}$ will be denoted as $Y_xCo_3(Ge_{1-y}Sn_y)_3$ and $Gd_xCo_3(Ge_{1-y}Sn_y)_3$, respectively.

2.3. Property Measurements. Temperature-dependent magnetization measurements were carried out for $T = 1.8$–300 K under

https://doi.org/10.1021/acs.inorgchem.3c02172
Inorg. Chem. 2023, 62, 18049−18055

magnetic fields of H = 0.1 T applied parallel (//) and perpendicular (⊥) to the crystallographic c-axis using a Quantum Design VSM Magnetic Property Measurement System. The specimens were attached to the quartz rods using GE-varnish. The isothermal magnetization measurements were also performed for H < 7 T. The specific heat (C) measurements were performed for T = 1.8−200 K in a Quantum Design Physical Properties Measurement System using a conventional thermal relaxation technique.

Electrical resistivity (ρ) measurements for $Y_xCo_3(Ge_{1-y}Sn_y)_3$ (x = 0.33, y = 0.11) over the temperature range of T = 1.8−300 K were performed in a four-wire configuration, where the platinum wires were spot-welded to the crystals in a standard four-wire configuration. The temperature dependence of resistivity of $Gd_xCo_3(Ge_{1-y}Sn_y)_3$ (x = 0.3, y = 0.133) was measured in an Oxford wet cryostat. The four-probe method with an AC current applied by a Zurich lock-in amplifier (MFLI) was used to measure the resistivity.

3. RESULTS AND DISCUSSION

3.1. Structure Determination. $Y_xCo_3(Ge_{1-y}Sn_y)_3$ (x = 0.33, y = 0.11) and $Gd_xCo_3(Ge_{1-y}Sn_y)_3$ (x = 0.3, y = 0.133) structures are best modeled in the hexagonal $P6/mmm$ space group with lattice parameters of a = 5.1185(1) Å × c = 3.9051(2) Å and a = 5.1239(6) Å × c = 3.9059(7) Å, respectively (Figure 2). The framework of alternating Co kagome and Ge honeycomb nets along the c-axis is ordered; however, the channels formed through the alignment of hexagonal voids host disordered "stuffing atoms". The stuffing atoms consist of Gd (planar to the honeycomb layer), Sn2 (planar to the kagome layer), and Ge2 (out of plane with the kagome layer by ∼0.20 Å above or below). The atoms within the channel can be best broken down into three disordered components. These disordered components are a pair of Gd−Ge2 dimers (each pair ∼30% occupied) and a lone ∼40% occupied Sn2 as shown in Figure 3. The occupancies of these components are constrained to a total occupancy of 100%. The $Ln_xCo_3(Ge_{1-y}Sn_y)_3$ structure is considered to be a hybrid of the CoSn and YCo_6Ge_6 structure types. The structure is reminiscent of CoSn when the Sn2 site is present and YCo_6Ge_6 when either of the two Gd−Ge2 dimers are present. The hybrid of the two structure types leads to the presence of disorder.

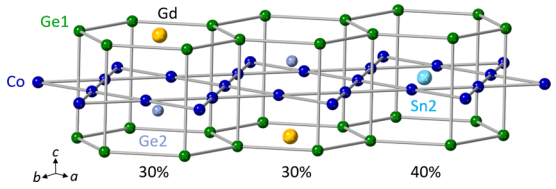

Figure 2. Crystal structure of $Gd_xCo_3(Ge_{1-y}Sn_y)_3$ and site symmetry of each atomic position.

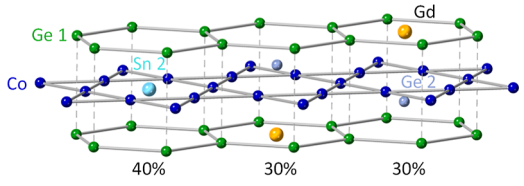

Figure 3. $Gd_xCo_3(Ge_{1-y}Sn_y)_3$ (x = 0.3, y = 0.133) structure is expanded to show the three random possible configurations of the disordered model. The percent occupancy of each configuration is provided. The dashed lines from Ge1−Ge1 are meant to guide the eye. Bonding between the Ge honeycomb nets and the Co kagome nets has been selectively omitted.

Of the LnM_6X_6 structure type, there are two major "stuffed" CoSn variants: the ordered $HfFe_6Ge_6$ [a = 5.069(1) Å, c = 8.041(1) Å][24] and the disordered YCo_6Ge_6 [a = 5.074 Å and c = 3.908 Å][25] structure types. Figure 4 shows the crystal structures of CoSn,[26] $HfFe_6Ge_6$, and YCo_6Ge_6 to provide a direct comparison between the related phases.

CoSn consists of alternating Sn honeycomb nets and Sn-centered Co kagome nets stacking along the c-axis. The alternating stacking nets form voids inside of a 20-atom polyhedron, as shown in Figure 5. The CoSn structure type, $(Co_3Sn)(Sn_2)$, can be divided into two alternating nets: the Co_3Sn kagome nets and the Sn_2 honeycomb nets. A Ge-doping study of the CoSn structure reveals that the site preference doping can lead to a doubling of the cell. The CoSn structure type is preserved when Ge is in the majority or Ge:Sn ratio of ∼2:1. The honeycomb nets only contain Ge. Sn is mixed with Ge in the plane of the Co kagome nets, which can be expressed as $(Co_3Sn_{1-y}Ge_y)(Ge_2)$. Conversely, when Sn is in the majority or a Sn:Ge ratio of ∼2:1, the c-axis of the CoSn structure type is doubled similar to what is observed in the $HfFe_6Ge_6$ structure type. Sn is mixed with Ge in the honeycomb nets, while only Sn is in the plane of the Co kagome nets and is classified as $(Co_3Sn)(Sn_{2-x}Ge_x)$. This implies that we can consider the site preference of Ge doping as a preference for kagome or honeycomb net structures. For our new hybrid analogues (Ln = Y and Gd), a rare earth site in the Ge_2 honeycomb nets is being filled up to a maximum of half occupied, which is observed in the YCo_6Ge_6 structure type. As the lanthanide site is being filled, the Sn site in the Co_3Sn kagome nets is displaced above and below the plane of the kagome nets. In our case, the displaced positions are "preferably" occupied by Ge instead of Sn.

While the CoSn structure type is widely viewed as the stuffed host for the LnM_6X_6 family, the CoGe binary is not isostructural. The ambient stable CoGe binary is a monoclinic distortion that breaks the kagome and honeycomb layers; however, it retains some of the motifs. The Sn-doping studies of the CoGe structure reveal the Sn site preference of the stuffing atom and stabilize the CoSn structure type.[27] Although it is unclear if the Sn doping in $Y_xCo_3(Ge_{1-y}Sn_y)_3$ (x = 0.33, y = 0.11) and $Gd_xCo_3(Ge_{1-y}Sn_y)_3$ (x = 0.3, y = 0.133) is a result of stability, it is interesting to note that the site preference is similar to that of its binary counterpart. Additionally, with the Sn substitution, we see that there is a stronger contribution of the CoSn structure type in the disorder compared to the undoped analogues. Y and Gd have Sn occupying the 1b in the CoSn component of the hybrid structure 33 and 30%, respectively, whereas the Yb analogue without Sn has a nearly negligible amount of Ge on the 1b site (∼8%). Seemingly, the incorporation of Sn in $Ln_xCo_3(Ge_{1-y}Sn_y)_3$ could be used as a tuning parameter to influence the hybrid structure's dominant component and possibly influence the amount of lanthanide stuffing. Although there is very little work done on $Yb_{0.5}Co_3(Ge_1Sn_y)_3$ structure types, we look to doping studies within the $HfFe_6Ge_6$ structure type to infer that the same type of doping is seen in ternary systems. Across multiple systems, there is a consistent site preference in small amounts of doping, where Sn prefers to dope within the stuffing atoms and Ge prefers the honeycomb net—consistent with our observation of doping.[28−30]

https://doi.org/10.1021/acs.inorgchem.3c02172
Inorg. Chem. 2023, 62, 18049−18055

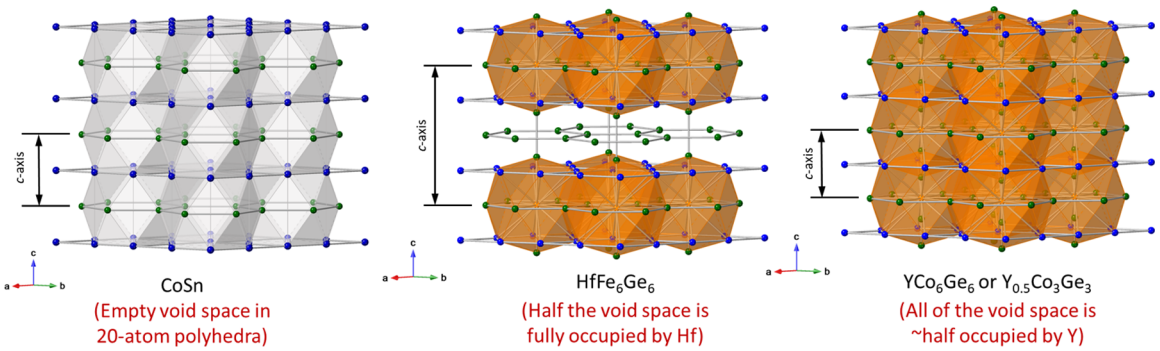

Figure 4. Structural comparison of CoSn [a = 5.2794(3) Å and c = 4.2598(3) Å], $HfFe_6Ge_6$ [a = 5.069(1) Å and c = 8.041(1) Å], and YCo_6Ge_6 [a = 5.074 Å and c = 3.908 Å]. For comparison, two unit cells of CoSn and YCo_6Ge_6 (stacked along the c-axis) are shown next to one unit cell $HfFe_6Ge_6$.

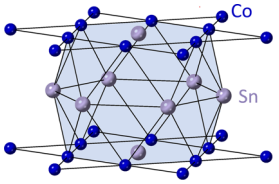

Figure 5. A 20-atom polyhedron serves as a void space in the CoSn structure type that is filled by Ln = alkali, alkaline earth, or lanthanide in the stuffed variants. Additional Co atoms are included to distinguish the contributing layers.

3.2. Physical Properties. The temperature-dependent magnetic susceptibility data for the nonmagnetic rare earth analogue $Y_xCo_3(Ge_{1-y}Sn_y)_3$ (x = 0.33, y = 0.11) were collected on single crystals. These data reveal that $Y_xCo_3(Ge_{1-y}Sn_y)_3$ (x = 0.33, y = 0.11) is a temperature-independent paramagnet and Co does not carry a magnetic moment (Figure S4). Figure 6a shows anisotropic magnetic susceptibility and inverse magnetic susceptibility data of $Gd_xCo_3(Ge_{1-y}Sn_y)_3$ (x = 0.3, y = 0.133), where the a- and c-axes have slightly different high-temperature behaviors. Unlike the previously reported data collected on polycrystalline $GdCo_6Ge_6$,[31] there is no magnetic ordering down to 1.8 K for a single crystal of $Gd_xCo_3(Ge_{1-y}Sn_y)_3$ (x = 0.3, y = 0.133). A Curie–Weiss fit to the data for temperatures T = 50–300 K yields an effective magnetic moment of μ_{eff} = 7.84(1) μ_B/Gd along the H//c direction and is consistent with the value expected for Gd^{3+} moment (μ_{eff} = 7.94 μ_B/Gd). However, an elevated μ_{eff} of 8.48 μ_B is seen for measurements along the H//a direction. The Weiss constants for H//a and H//c are −4.83 and 0.08 K, respectively, indicating antiferromagnetic interactions along the a-axis and little magnetic frustration as $\theta/T_N \sim 3$.[32] The low ordering temperature in the Gd analogue likely results from a weak magnetic exchange interaction between the Gd ions. The anisotropic field-dependent magnetization of $Gd_xCo_3(Ge_{1-y}Sn_y)_3$ (x = 0.3, y = 0.133), measured at T = 1.8 K, is shown in Figure 6b, where both curves rise rapidly and begin to saturate in the vicinity of 2 T. The saturation moment for H//a is approximately 6.6 μ_B, which is slightly less than a Gd^{3+} J = 7/2 system (M_{sat} = 7 μ_B/Gd). Along the c-axis, there is an elevated magnetic saturation moment of 7.9 μ_B, again implying that there is a magnetic contribution from the Co-kagome net: e.g., an elevated magnetic moment along the a-axis in comparison to the c-axis could indicate that the Co-magnetism occurs planar to the kagome net. While the origin of the magnetism in the Co sublattice is unknown, Co magnetism is not seen for other analogues[15,16,31] and CoSn (and Ge-doped analogues),[27,33] and we speculate that the presence may be due to the impact of the Gd f-state on the electronic band structure. Further work (e.g., electronic structure calculations or a more systematic study of other Ln variants) is needed to answer this question.

Figure 7a shows the temperature-dependent heat capacity of $Y_xCo_3(Ge_{1-y}Sn_y)_3$ (x = 0.33, y = 0.11) and $Gd_xCo_3(Ge_{1-y}Sn_y)_3$ (x = 0.3, y = 0.133) measured at H = 0 T with a temperature range of 0.5–200 K. Both the Sommerfeld coefficients and the Debye temperatures were determined by fitting the data using

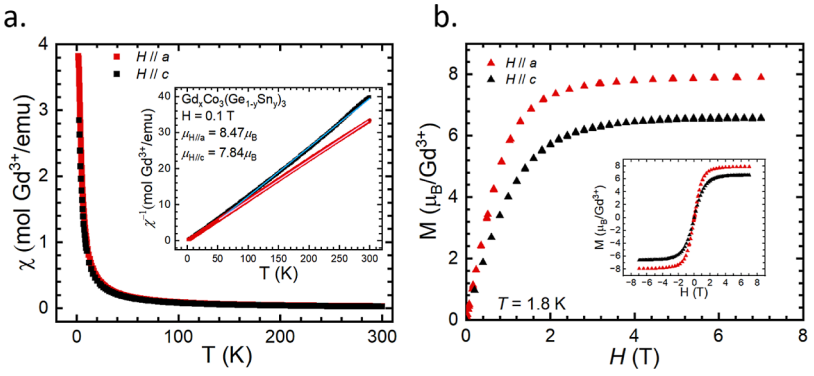

Figure 6. Anisotropic magnetic measurements of $Gd_xCo_3(Ge_{1-y}Sn_y)_3$. (a) Temperature-dependent magnetic susceptibility, χ(T), collected for temperature T = 1.8–300 K. (Inset) The Curie–Weiss fits were applied to inverse susceptibility, χ^{-1}, as described in the text and are represented by solid lines. (b) Anisotropic field-dependent magnetization, $M(H)$, collected at T = 1.8 K and for −7 < H < 7 T.

https://doi.org/10.1021/acs.inorgchem.3c02172
Inorg. Chem. 2023, 62, 18049–18055

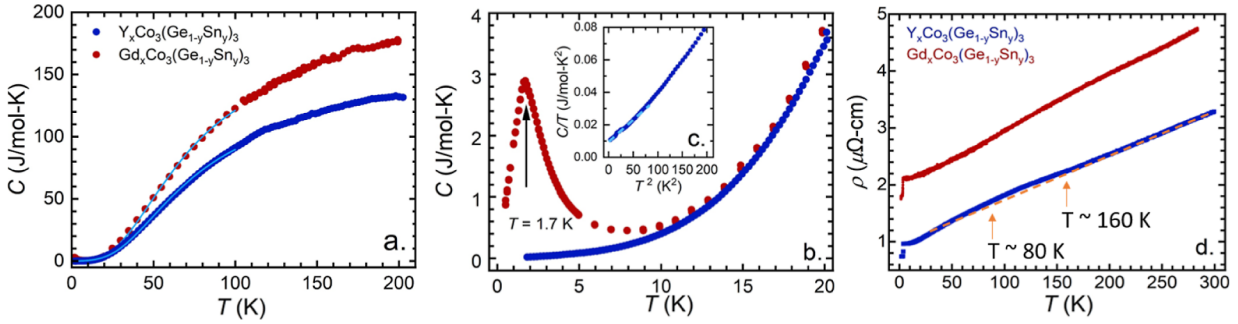

Figure 7. (a) Temperature-dependent heat capacity, $C(T)$, of both the Y and Gd analogues. A subtle kink in the heat capacity is seen at $T \sim 118$ K, as indicated by an arrow. The light blue dashed line represents the integral Debye fit, as described in the text. (b) The low-temperature region heat capacity shows a magnetic phase transition occurring at $T = 1.7$ K for the Gd analogue. (c) Heat capacity divided by temperature, C/T vs T^2, for $Y_xCo_3(Ge_{1-y}Sn_y)_3$ ($x = 0.33$, $y = 0.11$). The dotted line is a fit to the data using the expression $\frac{C}{T} = \gamma + \beta T^2$. (d) Temperature-dependent electrical resistivity, $\rho(T)$, for $Y_xCo_3(Ge_{1-y}Sn_y)_3$ ($x = 0.33$, $y = 0.11$) and $Gd_xCo_3(Ge_{1-y}Sn_y)_3$ ($x = 0.3$, $y = 0.133$), where metallic behavior is observed. The dotted line in orange is a linear fit to highlight a broad feature spanning ~80 to 160 K. The drop in resistivity at ~3 K is due to Sn inclusions.

the expression $C_p = \gamma T + C_{Debye}$ (solid lines), where γT is the electronic contribution and C_{Debye} is the integral Debye function. The Sommerfeld coefficients for both analogues were found to be near 9.0 mJ/mol K^2, and the Debye temperatures are $\theta_Y = 298$ K and $\theta_{Gd} = 289$ K. The fitting ranges between the Y and Gd analogues vary slightly due to the low-temperature magnetic ordering, as seen in $Gd_xCo_3(Ge_{1-y}Sn_y)_3$ ($x = 0.3$, $y = 0.133$) shown in Figure 7b. A linear fit at the low temperatures of $Y_xCo_3(Ge_{1-y}Sn_y)_3$ ($x = 0.33$, $y = 0.11$) T vs T^2 (Figure 7c) yielded $\gamma = 9$ mJ/mol K^2 and $\beta = 0.26$ mJ/mol K^4, consistent with the results from the integral Debye fit. In the heat capacity of $Y_xCo_3(Ge_{1-y}Sn_y)_3$, there also is a weak kink at $T \sim 118$ K, possibly representing a phase transition that is reminiscent of what is seen in $MgCo_6Ge_6$ and $Yb_{0.5}Co_3Ge_3$.[18,21] For those compounds, kinks are also seen in the resistivity and have been shown to be related to a structural phase transition. However, for $Y_xCo_3(Ge_{1-y}Sn_y)_3$ ($x = 0.33$, $y = 0.11$), low-temperature single-crystal X-ray diffraction data were collected down to 90 K and provided no indication of a phase transition (Tables S3 and S4). In the Gd analogue, the low-temperature heat capacity measurements reveal a broad peak at $T = 1.7$ K, which indicates magnetic ordering. At higher temperatures, the heat capacities of the Y and Gd analogues have different behaviors, possibly indicating different phonon interactions or the presence of an itinerant cobalt magnetic contribution that was not observed in the Y analogue. Alternatively, changes in the disorder occupancy could lead to the change of phonon modes; however, the measurement of other lanthanide analogues is required to establish a trend. Figure 7b shows the electrical resistivity as a function of temperature. Also noteworthy is that $\rho(T)$ for single crystalline of $Y_xCo_3(Ge_{1-y}Sn_y)_3$ ($x = 0.33$, $y = 0.11$) is lower by an order of magnitude than previously reported polycrystalline samples that were produced by arc melting.[15] Conventional metallic behavior is observed over the entire temperature range for both compounds. Interestingly, there is a broad hump in $\rho(T)$ apexing near $T = 120$ K for the Y compound that roughly coincides with the feature that is seen in C/T. While this does not definitively establish the presence of a phase transition, the positive curvature is consistent with weak and gradual gapping of the Fermi energy. Finally, the sudden decrease of resistivity at ~3 K is due to Sn inclusions; Sn contains a superconducting transition temperature of 3.7 K.[34]

4. CONCLUSIONS

Herein, we are reporting the new hybrid structures $Y_xCo_3(Ge_{1-y}Sn_y)_3$ ($x = 0.33$, $y = 0.11$) and $Gd_xCo_3(Ge_{1-y}Sn_y)_3$ ($x = 0.3$, $y = 0.133$) with Sn incorporation that could ignite the investigation of Sn analogues and doping studies and invite the reinvestigation of other lanthanide analogues. The growth of single crystals allowed novel anisotropic magnetic measurements that reveal exclusive Co magnetic contribution along H//a in the Gd analogue, which is in-plane with the kagome net. The magnetic properties for the nonmagnetic Y analogue do not contain Co contributions, which we speculate could be due to the impact of Gd f-electrons. In addition to magnetic measurements, the heat capacity study also revealed a low-temperature magnetic transition at ~1.7 K in the Gd analogue; this transition, coupled with the insights of electronic kagome features, could result in new exotic states, justifying further theoretical and experimental investigations.

The ability to tune magnetism in the $Ln_xCo_3(Ge_{1-y}Sn_y)_3$ family with a twist distortion,[35−37] similar to the superconducting $LaRu_3Si_2$ family, makes the nonmagnetic analogue a great platform to study the interplay of magnetism correlation. The kagome net means that magnetism has to deal with the electronic correlation in the system. Furthermore, this work illustrates the family of $Ln_xCo_3(Ge_{1-y}Sn_y)_3$ as a special platform to further investigate the interplay of magnetism and correlation and invites the discovery of structures of the $Ln_xCo_3(Ge_{1-y}Sn_y)_3$ type, where related structural complexity and magnetism are best elucidated via growth of large single crystals. We expect that new materials will advance the understanding of the interplay of electronic correlation, topology, and magnetism in these kagome compounds. The observation of magnetic ordering in an inherent topological kagome lattice would warrant further investigation of its effects on the band structure through theoretical and experimental methods.

■ ASSOCIATED CONTENT

Supporting Information

The Supporting Information is available free of charge at https://pubs.acs.org/doi/10.1021/acs.inorgchem.3c02172.

Crystallographic data and refinement parameters of $Y_xCo_3(Ge_{1-y}Sn_y)_3$ and $Gd_xCo_3(Ge_{1-y}Sn_y)_3$; selected interatomic distances of $Y_xCo_3(Ge_{1-y}Sn_y)_3$ and $Gd_xCo_3(Ge_{1-y}Sn_y)_3$; low-temperature crystallographic

https://doi.org/10.1021/acs.inorgchem.3c02172
Inorg. Chem. 2023, 62, 18049−18055

data and refinement parameters of $Y_xCo_3(Ge_{1-y}Sn_y)_3$; low-temperature (T = 90 K) atomic coordinates of $Y_xCo_3(Ge_{1-y}Sn_y)_3$; X-ray powder refinement results for $Y_xCo_3(Ge_{1-y}Sn_y)_3$; X-ray Rietveld refinement results for $Gd_xCo_3(Ge_{1-y}Sn_y)_3$; precession images of $Y_xCo_3(Ge_{1-y}Sn_y)_3$ and $Gd_xCo_3(Ge_{1-y}Sn_y)_3$; magnetic susceptibility and inverse magnetic susceptibility of $Y_xCo_3(Ge_{1-y}Sn_y)_3$; Fourier maps; and crystal structure of AB_6X_6 (PDF)

Accession Codes

CCDC 2254793−2254794 contain the supplementary crystallographic data for this paper. These data can be obtained free of charge via www.ccdc.cam.ac.uk/data_request/cif, or by emailing data_request@ccdc.cam.ac.uk, or by contacting The Cambridge Crystallographic Data Centre, 12 Union Road, Cambridge CB2 1EZ, UK; fax: +44 1223 336033.

AUTHOR INFORMATION

Corresponding Author

Julia Y. Chan − *Department of Chemistry and Biochemistry, Baylor University, Waco, Texas 76798, United States;* orcid.org/0000-0003-4434-2160; Email: Julia_Chan@baylor.edu

Authors

Moisés Bravo − *Department of Chemistry and Biochemistry, Baylor University, Waco, Texas 76798, United States;* orcid.org/0000-0002-1846-4618

Gregory T. McCandless − *Department of Chemistry and Biochemistry, Baylor University, Waco, Texas 76798, United States*

Ryan E. Baumbach − *National High Magnetic Field Laboratory, Florida State University, Tallahassee, Florida 32310, United States*

Yaojia Wang − *Kavli Institute of Nanoscience, Delft University of Technology, Delft 2628 CJ, The Netherlands; Department of Chemistry and Biochemistry, Baylor University, Waco, Texas 76798, United States*

Mazhar N. Ali − *Kavli Institute of Nanoscience, Delft University of Technology, Delft 2628 CJ, The Netherlands; Department of Chemistry and Biochemistry, Baylor University, Waco, Texas 76798, United States*

Complete contact information is available at: https://pubs.acs.org/10.1021/acs.inorgchem.3c02172

Notes

The authors declare no competing financial interest.

ACKNOWLEDGMENTS

R.B. is supported by the National Science Foundation through NSF DMR-1904361. The National High Magnetic Field Laboratory is supported by the National Science Foundation through NSF DMR-1644779 and the State of Florida. Y.W. acknowledges the support from the NWO Talent Programme Veni financed by the Dutch Research Council (NWO), project no. VI.Veni.212.146. Y.W. and M.N.A. acknowledge support from the Technical University of Delft Quantum Nanoscience Department and Kavli Institute of Nanoscience Delft. Work at Baylor was supported by the National Science Foundation through NSF DMR 2209804 and the Welch Foundation through AT-2056-20220101.

REFERENCES

(1) Yin, J.-X.; Lian, B.; Hasan, M. Z. Topological Kagome Magnets and Superconductors. *Nature* **2022**, *612*, 647−657.

(2) Wang, Y.; Wu, H.; McCandless, G.; Chan, J.; Ali, M.. Quantum States and Intertwining Phases in Kagome Materials. *Nat. Rev. Phys.***2023**, arXiv:2303.03359.

(3) Brabers, J. H. V. J.; Duijn, V. H. M.; de Boer, F. R.; Buschow, K. H. J. Magnetic Properties of Rare-Earth Manganese Compounds of the RMn_6Ge_6 Type. *J. Alloys Compd.* **1993**, *198*, 127−132.

(4) Wang, Y. B.; Wiards, D.; Ryan, D. H.; Cadogan, J. M. Structural and Magnetic Properties of RFe_6Ge_6 (R = Y, Gd, Tb, Er). *IEEE Trans. Magn.* **1994**, *30*, 4951−4953.

(5) Venturini, G.; Welter, R.; Malaman, B. Crystallographic Data and Magnetic Properties of RT_6Ge_6 Compounds (R= Sc, Y, Nd, Sm, Gd-Lu; T = Mn, Fe). *J. Alloys Compd.* **1992**, *185*, 99−107.

(6) Liu, C.; Zhang, H.; Li, Z.; Yan, Y.; Zhang, Y.; Hou, Z.; Fu, X. Nontrivial Spin Textures Induced Remarkable Topological Hall Effect and Extraordinary Magnetoresistance in Kagome Magnet $TmMn_6Sn_6$. *Surface. Interfac.* **2023**, *39*, 102866.

(7) Yin, J.-X.; Ma, W.; Cochran, T. A.; Xu, X.; Zhang, S. S.; Tien, H.-J.; Shumiya, N.; Cheng, G.; Jiang, K.; Lian, B.; Song, Z.; Chang, G.; Belopolski, I.; Multer, D.; Litskevich, M.; Cheng, Z.-J.; Yang, X. P.; Swidler, B.; Zhou, H.; Lin, H.; Neupert, T.; Wang, Z.; Yao, N.; Chang, T.-R.; Jia, S.; Zahid Hasan, M. Quantum-limit Chern Topological Magnetism in $TbMn_6Sn_6$. *Nature* **2020**, *583*, 533−536.

(8) Venturini, G.; Fruchart, D.; Malaman, B. Incommensurate Magnetic Structures of RMn_6Sn_6 (R = Sc, Y, Lu) Compounds From Neutron Diffraction Study. *J. Alloys Compd.* **1996**, *236*, 102−110.

(9) Zhang, H.; Liu, C.; Zhang, Y.; Hou, Z.; Fu, X.; Zhang, X.; Gao, X.; Liu, J. Magnetic Field-induced Nontrivial Spin Chirality and Large Topological Hall Effect in Kagome Magnet $ScMn_6Sn_6$. *Appl. Phys. Lett.* **2022**, *121*, 202401.

(10) Venturini, G.; Idrissi, B. E.; Malaman, B. Magnetic Properties of RMn_6Sn_6 (R = Sc, Y, Gd-Tm, Lu) Compounds with $HfFe_6Ge_6$- Type Structure. *J. Magn. Magn. Mater.* **1991**, *94*, 35−42.

(11) Venturini, G.; Welter, R.; Malaman, B.; Ressouche, E. Magnetic Structure of YMn_6Ge_6 and Room Temperature Magnetic Structure of $LuMn_6Sn_6$ Obtained From Neutron Diffraction Study. *J. Alloys Compd.* **1993**, *200*, 51−57.

(12) Pokharel, G.; Teicher, S. M. L.; Ortiz, B. R.; Sarte, P. M.; Wu, G.; Peng, S.; He, J.; Seshadri, R.; Wilson, S. D. Electronic Properties of the Topological Kagome Metals YV_6Sn_6 and GdV_6Sn_6. *Phys. Rev. B* **2021**, *104*, 235139.

(13) Arachchige, H. W. S.; Meier, W. R.; Marshall, M.; Matsuoka, T.; Xue, R.; McGuire, M. A.; Hermann, R. P.; Cao, H.; Mandrus, D. Charge Density Wave in Kagome Lattice Intermetallic ScV_6Sn_6. *Phys. Rev. Lett.* **2022**, *129*, 216402.

(14) Guo, K.; Ye, J.; Guan, S.; Jia, S. Triangular Kondo Lattice in YbV_6Sn_6 and Its Quantum Critical Behavior in a Magnetic Field. *Phys. Rev. B* **2023**, *107*, 205151.

(15) Fedyna, M. F.; Skolozdra, R. V.; Gorelenko, Y. K. Magnetic and Electric Properties of RCo_6Ge_6 (R = Y, Dy, Er-Lu). *Neorg. Mater.* **1999**, *35*, 461−463.

(16) Skolozdra, R. V.; Koretskaya, O. E. Crystal Structure and Magnetic Susceptibility of the Stannides RCo_6Sn_6 (R = Yttrium, Terbium, Dysprosium, Holmium, Erbium, Thulium, Lutetium). *Ukr. J. Phys. Opt.* **1984**, *29*, 877−879.

(17) Weiland, A.; Eddy, L. J.; McCandless, G. T.; Hodovanets, H.; Paglione, J.; Chan, J. Y. Refine Intervention: Characterizing Disordered $Yb_{0.5}Co_3Ge_3$. *Cryst. Growth Des.* **2020**, *20*, 6715−6721.

(18) Wang, Y.; McCandless, G. T.; Wang, X.; Thanabalasingam, K.; Wu, H.; Bouwmeester, D.; van der Zant, H. S. J.; Ali, M. N.; Chan, J. Y. Electronic Properties and Phase Transition in the Kagome Metal $Yb_{0.5}Co_3Ge_3$. *Chem. Mater.* **2022**, *34*, 7337−7343.

(19) Teng, X.; Chen, L.; Ye, F.; Rosenberg, E.; Liu, Z.; Yin, J.-X.; Jiang, Y.-X.; Oh, J. S.; Hasan, M. Z.; Neubauer, K. J.; Gao, B.; Xie, Y.; Hashimoto, M.; Lu, D.; Jozwiak, C.; Bostwick, A.; Rotenberg, E.; Birgeneau, R. J.; Chu, J.-H.; Yi, M.; Dai, P. Discovery of Charge

Density Wave in a Kagome Lattice Antiferromagnet. *Nature* **2022**, *609*, 490−495.
(20) Luo, H.; Gao, Q.; Liu, H.; Gu, Y.; Wu, D.; Yi, C.; Jia, J.; Wu, S.; Luo, X.; Xu, Y.; Zhao, L.; Wang, Q.; Mao, H.; Liu, G.; Zhu, Z.; Shi, Y.; Jiang, K.; Hu, J.; Xu, Z.; Zhou, X. J. Electronic Nature of Charge Density Wave and Electron-Phonon Coupling in Kagome Superconductor KV_3Sb_5. *Nat. Commun.* **2022**, *13*, 273.
(21) Sinha, M.; Vivanco, H. K.; Wan, C.; Siegler, M. A.; Stewart, V. J.; Pogue, E. A.; Pressley, L. A.; Berry, T.; Wang, Z.; Johnson, I.; Chen, M.; Tran, T. T.; Phelan, W. A.; McQueen, T. M. Twisting of 2D Kagomé Sheets in Layered Intermetallics. *ACS Cent. Sci.* **2021**, *7*, 1381−1390.
(22) Krause, L.; Herbst-Irmer, R.; Sheldrick, G. M.; Stalke, D. Comparison of Silver and Molybdenum Microfocus X-ray Sources For Single-Crystal Structure Determination. *J. Appl. Crystallogr.* **2015**, *48*, 3−10.
(23) Sheldrick, G. M. *SHELXT*- Integrated Space-Group and Crystal-Structure Determination. *Acta Crystallogr., Sect. A: Found. Adv.* **2015**, *71*, 3−8.
(24) Olenych, R. R.; Aksel'rud, L. G.; Yarmolyuk, Y. P. Crystal Structure of Ternary Germanides RFe_6Ge_6 (R= Sc, Ti, Zr, Hf, Nb) and RCo_6Ge_6 (R= Ti, Zr, Hf). *Dopov. Akad. Nauk Ukr. RSR, Ser. A: Fiz.-Mat. Tekh. Nauki* **1981**, *43*, 84−88.
(25) Buchholz, W.; Schuster, H.-U. Intermetallische Phasen mit B35-Überstruktur und Verwandtschaftsbeziehung zu $LiFe_6Ge_6$. *Z. Anorg. Allg. Chem.* **1981**, *482*, 40−48.
(26) Rüdorff, W.; Hofmann, U. Über Graphitsalze. *Z. Anorg. Allg. Chem.* **1938**, *238*, 1−50.
(27) Allred, J. M.; Jia, S.; Bremholm, M.; Chan, B. C.; Cava, R. J. Ordered CoSn-type Ternary Phases in $Co_3Sn_{3-x}Ge_x$. *J. Alloys Compd.* **2012**, *539*, 137−143.
(28) Venturini, G. Crystallographic and Magnetic Properties of $HfFe_6Ge_6$-type $REFe_6Sn_4Ge_2$ Compounds (RE = Y, Gd-Er). *J. Alloys Compd.* **2005**, *400*, 37−42.
(29) Perry, L. K.; Ryan, D. H.; Venturini, G.; Malaman, B. $LFe_6Sn_4Ge_2$ (L = Dy, Ho, Er) Studied by Neutron Diffraction and Mössbauer Spectroscopy. *J. Alloys Compd.* **2009**, *486*, 29−36.
(30) Mazet, T.; Ihou-Mouko, H.; Ryan, D. H.; Voyer, C. J.; Cadogan, J. M.; Malaman, B. Valence Change and Magnetic Order in $YbMn_6Ge_{6-x}Sn_x$. *J. Phys.: Condens. Matter* **2010**, *22*, 116005.
(31) Szytuła, A.; Wawrzyńska, E.; Zygmunt, A. Crystal Structure and Magnetic Properties of $GdCo_6X_6$ (X = Ge, Sn) and $TbCo_6Ge_6$. *J. Alloys Compd.* **2004**, *366*, L16−L18.
(32) Balents, L. Spin liquids in frustrated magnets. *Nature* **2010**, *464*, 199−208.
(33) Kang, M.; Fang, S.; Ye, L.; Po, H. C.; Denlinger, J.; Jozwiak, C.; Bostwick, A.; Rotenberg, E.; Kaxiras, E.; Checkelsky, J. G.; Comin, R. Topological Flat Bands in Frustrated Kagome Lattice CoSn. *Nat. Commun.* **2020**, *11*, 4004.
(34) Eisenstein, J. Superconducting Elements. *Rev. Mod. Phys.* **1954**, *26*, 277−291.
(35) Mielke, C.; Qin, Y.; Yin, J. X.; Nakamura, H.; Das, D.; Guo, K.; Khasanov, R.; Chang, J.; Wang, Z. Q.; Jia, S.; Nakatsuji, S.; Amato, A.; Luetkens, H.; Xu, G.; Hasan, M. Z.; Guguchia, Z. Nodeless Kagome Superconductivity in $LaRu_3Si_2$. *Phys. Rev. Mater.* **2021**, *5*, 034803.
(36) Chakrabortty, S.; Kumar, R.; Mohapatra, N. Effect of Tunable Spin-orbit Coupling on the Superconducting Properties of $LaRu_3Si_2$ Containing Kagome-honeycomb Layers. *Phys. Rev. B* **2023**, *107*, 024503.
(37) Li, S.; Tao, J.; Wan, X.; Ding, X.; Yang, H.; Wen, H.-H. Distinct Behaviors of Suppression to Superconductivity in $LaRu_3Si_2$ Induced by Fe and Co Dopants. *Phys. Rev. B: Condens. Matter Mater. Phys.* **2012**, *86*, 024513.

https://doi.org/10.1021/acs.inorgchem.3c02172
Inorg. Chem. 2023, 62, 18049−18055